CONCENTRATION OF THE SPECIFIC ABSORPTION RATE AROUND DEEP BRAIN STIMULATION ELECTRODES DURING MRI

S. A. Mohsin[*]

Department of Electrical Engineering, University of Faisalabad, Faisalabad, Pakistan

Abstract—During Magnetic Resonance Imaging (MRI), the presence of an implant such as a Deep Brain Stimulation (DBS) lead in a patient's body can pose a significant risk. This is due to the fact that the MR radiofrequency (RF) field can achieve a very high strength around the DBS electrodes. Thus the specific absorption rate (SAR), which is proportional to the square of the magnitude of the RF electric field, can have a very high concentration in the near-field region of the electrodes. The resulting tissue heating can reach dangerous levels. The degree of heating depends on the level of SAR concentration. The effects can be severe, leading to tissue ablation and brain damage, and significant safety concerns arise whenever a patient with an implanted DBS lead is exposed to MR scanning. In this paper, SAR, electric field, and temperature rise distributions have been found around actual DBS electrodes. The magnitude and spatial distribution of the induced temperature rises are found to be a function of the length and structure of the lead device, tissue properties and the MR stimulation parameters.

1. INTRODUCTION

Magnetic Resonance Imaging is a vital medical imaging modality and is widely used for diagnostic and interventional procedures because of its noninvasive and nonionising nature. For example, MRI images of the brain can yield valuable diagnostic information [1]. Many psychiatric disorders are caused by abnormal brain function and are treated using deep brain stimulation (DBS) leads that have stimulation electrodes embedded deep inside brain tissue. Fig. 1 shows a DBS lead implant in

a patient. The lead is implanted just below the skin of the upper chest, side of the neck, and head where it then runs deep into the brain. At one end of the lead (beneath the skin of the chest), there is small pulse generator and at the other end are the DBS electrodes. MRI is used for the placement of the electrodes and subsequently for monitoring the progress of patients [2, 3]. All electromagnetic (EM) fields affect biological tissue and vice versa [4–7], and the powerful EM fields used in MRI systems are no exception. At the usual strengths used for imaging, the MRI EM fields by themselves are not hazardous to human tissue because the resultant fields do not achieve high strength levels in tissue. However, when an implanted medical device such as a DBS lead is present inside tissue, the situation changes. This is because the MRI fields are affected by the presence of the implanted device and the resultant fields' distributions in the presence of an implanted device can be much different than those in the absence of such a device: high strength levels in specific tissue regions can be achieved. Thus the use of MRI on patients with implanted DBS leads is an important safety issue. The EM fields used for imaging in a MRI unit are: a static magnetic field, gradient magnetic fields, and an RF field [8]. The different MRI fields interact in different ways with different implanted devices. The static and gradient magnetic fields show no hazardous interaction with an implanted device made of nonmagnetic materials, but the RF field can be scattered significantly by an implanted device, especially one that contains metal parts. The scattered RF field can have a very high strength, and will produce conduction currents in the tissue immediately surrounding the implanted device. The currents will cause resistive heating that can be potentially hazardous. DBS leads consist of metal wires that are insulated along their entire length except for bare electrodes at one end. When subjected to an RF field, the scattered RF wave propagates in the thin insulation sheath. The energy is carried to the tissue surrounding the electrodes, and thus the most intense field is produced there. The specific absorption rate (SAR in W/kg), is the rate at which heat is absorbed per unit mass of tissue. The local SAR is proportional to the square of the magnitude of the electric field and thus there is a SAR concentration in the tissue near the electrodes. This local SAR is many orders of magnitude greater than the local SAR produced in human tissue due to many other common RF applications such as cellular phones [9–11]. The local temperature rise in the tissue surrounding the electrodes can reach very dangerous levels. The local nature of the dangerous effect means that a whole-body averaged SAR value, [12], will not be useful in determining the local effect: It is the local SAR distribution that is more important.
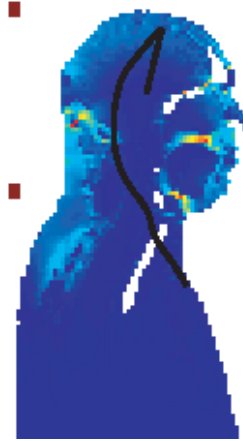
Figure 1. A DBS lead implanted in a patient. The lead runs from the chest (beneath the skin) along the neck to the top of the scalp and then deep into brain tissue. The DBS electrodes, at the end of the lead in the brain, are too small to show in this figure.

Although the heating effect is primarily in the tissue near the electrodes, and the nature of this tissue is certainly important, yet the nature of the tissue in which the connecting portion of the lead is embedded and the length of the entire lead are also important. The nature of the tissue determines the resonant length of a lead and the closer the actual length is to the resonant length, the greater the induced heating will be. The interested reader is referred to Mohsin et al. [13] for the details. In the present paper, we examine the induced heating around actual lead electrodes. The leads selected for this purpose are the Medtronic 3387 and 3389 leads (Medtronic Inc., Minneapolis, MN, USA). We examine two different lengths of each lead. DBS electrodes have been modeled by various researchers [13–15], by removing the insulation from one end of the inner metallic conductor; however exact electrode shapes have not been modeled due to their complicated structure. We compute the SAR and temperature rise distributions around the exact electrode structures.

2. SPECIFICATION AND PLACEMENT

The connecting portion of each lead consists of four very thin individually insulated metallic wires covered by a (collective) insulating sheath having an outer diameter of 1.27 mm. In the 3387 lead, the

four insulated wires are tightly coiled around each other while in the
3389 lead they run parallel to each other. At MRI radiofrequencies,
the strands can be modeled by a single metallic strand 0.7 mm in
diameter covered by the insulating sheath having an outer diameter
of 1.27 mm. This inner metallic strand and its insulation sheath have
been collectively referred to as the "connecting portion" in Fig. 2.
The connecting portion serves to convey the electric potential pulses
produced by an implantable pulse generator to the DBS electrodes.
The connecting portion is long and typical lengths range from 50 cm
to 70 cm; thus in Fig. 2, according to the scale of the figure, only a
small ending length of the connecting part terminating in the DBS
electrodes is shown. Fig. 2 also shows the four platinum-iridium
metallic electrodes, the insulations separating them, and the ending
rounded insulation tip; all these parts are collectively referred to as
the "electrodes' portion" here. The overall length of the electrodes'
portion is 1.2 cm for the 3387 lead and 0.9 cm for the 3389 lead.
The diameter of each of the four metal electrodes and the insulating
portions separating them is 1.27 mm. Thus the outer surface of the
insulation of the connecting portion is flush with the outer surface of
the proximal electrode. Both leads possess cylindrical symmetry and
the central cylindrical axis running along the center of each lead is
called the x-axis here (see Fig. 2); the distance measured along this
axis is x and $x = 0$ at the distal end (rounded insulated tip) of the
electrodes portion. The value of x increases towards the proximal end
of the electrodes portion. However, x decreases from zero to more
negative values as we move away from the distal end into brain tissue.
For the 3387 lead, the electrodes extend from $x = 0$ to 12 mm; for the
3389 lead, the electrodes extend from $x = 0$ to 9 mm. The distance
measured radially away from the central cylindrical axis is r. Thus
$r = 0$ at every point lying on the x–axis (the x-axis is the $r = 0$ axis),
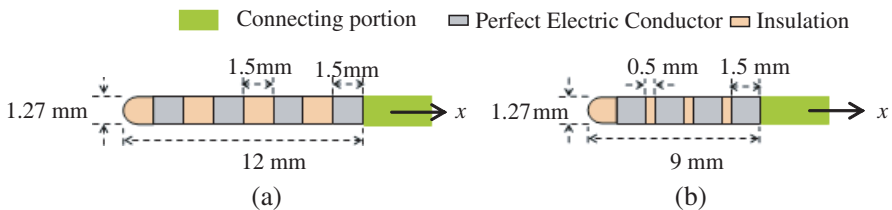
Figure 2. Electrodes of: (a) 3387 Lead (b) 3389 Lead. The connecting
part of the lead is covered by an insulating sheath, the outer surface
of which is flush with the electrodes' surface. The central cylindrical
axis of each lead is the x-axis.

and the center of the distal end of the electrodes' portion, that is, the tip of the rounded insulation forming the distal end of the electrodes' portion in Fig. 2 is at the point $(r, x) = (0, 0)$. Five cm of each lead at the electrodes end is embedded in brain tissue having conductivity, $\sigma = 0.47\,\mathrm{S/m}$ and relative permittivity, $\varepsilon_r = 80$; the rest of the lead is in tissue with fat content having $\sigma = 0.1\,\mathrm{S/m}$ and $\varepsilon_r = 10$. The lead is placed so that its center (lengthwise) is at the landmark, that is, the center of the MRI RF birdcage coil. The MRI system is rated at 1.5 Teslas having a radiofrequency of 64 MHz. The MRI input power is such that the RF electric field strength is 100 V/m at the landmark. In the vicinity of the landmark, the amplitude of the field is almost constant along the axis of the coil. The background SAR in muscle is 2.35 W/kg, and in fat is 0.5 W/kg. The symbols used to identify the leads that have been analyzed are:

L_1: 3387 lead, length 25 cm
L_2: 3387 lead, length 48 cm
L_3: 3389 lead, length 25 cm
L_4: 3389 lead, length 41 cm

3. COMPUTATION OF THE RESULTANT RF FIELD

The scattered RF field that exists inside tissue can be computed using one of the many EM computational methods that are available. These
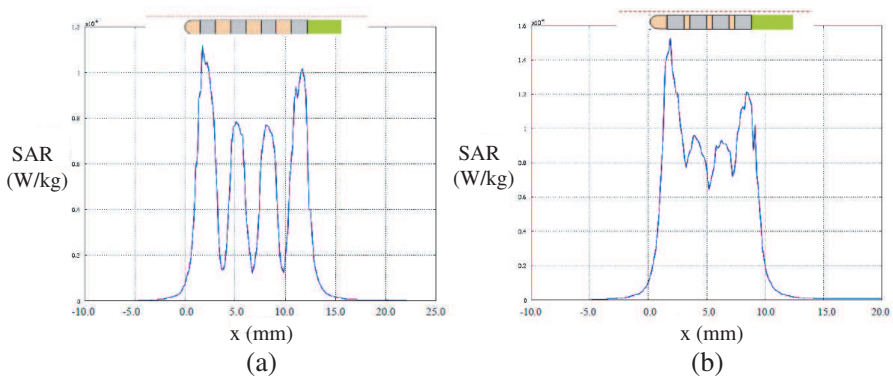
Figure 3. Local SAR plot against distance along a line (shown in dotted red, parallel to the electrodes, at the top of each plot). The line is at a distance of 0.5 mm from the electrodes' surface, i.e., the line is at $r = 0.635\,\mathrm{mm} + 0.5\,\mathrm{mm}$. (a) L_2. (b) L_4.

include the method of moments [16], the finite difference time domain method, (FDTD) [17, 18], the finite element method (FEM) [19, 20], and various other ingenious methods [21]. Here, for computational simplicity and for keeping the size of the computational problem small, we solve the problem in two stages [22]. In the first stage, the RF field that exists in the interior of the MRI birdcage coil in the presence of body tissue with *no implants present* was computed using the FDTD method [23, 24]. The computed field was available as matrix data. A very reasonable approximation is that the presence of an implant has a negligible effect on the MRI RF source (that is, the birdcage coil) [22, 25]. Therefore the RF field computed in the presence of body tissue but in the absence of any implants can be used as the incident field when one or more implants are present. This incident field $(\mathbf{E}^i, \mathbf{H}^i)$ that exists inside body tissue (in the MRI chamber)
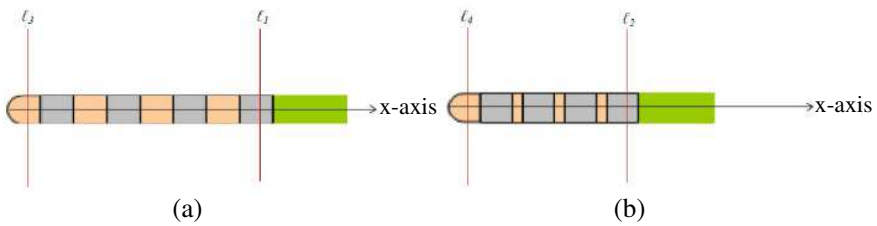
Figure 4. Specification of radial lines for SAR plots. (a) 3387 electrodes. (b) 3389 electrodes.
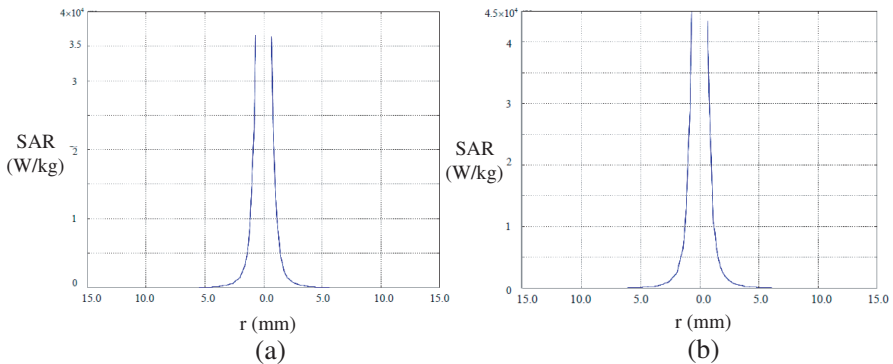
Figure 5. Plots of the local SAR against distance measured along a radial line crossing a metal electrode. (a) The lead is $\mathbf{L}_2$ and the radial line is ℓ_1. (b) The lead is $\mathbf{L}_4$ and the radial line is ℓ_2. See Fig. 4 for the meaning of ℓ_1 and ℓ_2.

satisfies the wave equation

$$\vec{\nabla} \times \vec{\nabla} \times \mathbf{E}^i + j\omega\mu_0 \left(\sigma + j\omega\varepsilon\right) \mathbf{E}^i = 0 \tag{1}$$

and $\mathbf{H}^i$ is given by the Maxwell's equation, $\mathbf{H}^i = \{-1/(j\omega\mu_0)\}\vec{\nabla} \times \mathbf{E}^i$, where σ, ε, and μ_0 are the electrical conductivity, electrical permittivity, and magnetic permeability respectively of tissue. The permeability is a constant equal to the permeability of free space while σ and ε are in general functions of position. The resultant, that is, the
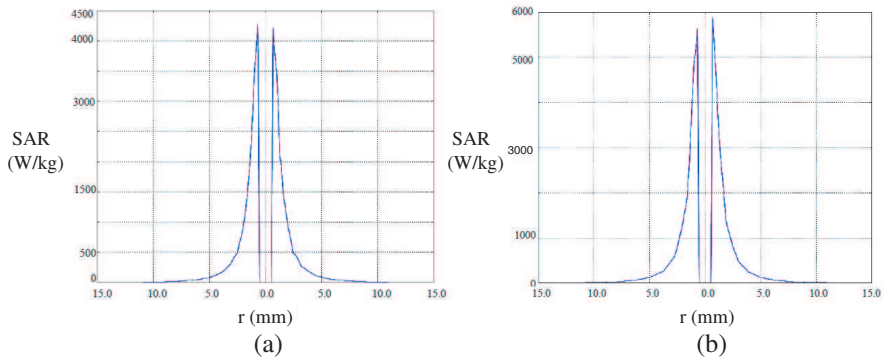
Figure 6. Plots of the local SAR against distance measured along a radial line crossing the insulated tip of the electrodes' portion. (a) The lead is $\mathbf{L}_2$ and the radial line is ℓ_3. (b) The lead is $\mathbf{L}_4$ and the radial line is ℓ_4. See Fig. 4 for the meaning of ℓ_3 and ℓ_4.
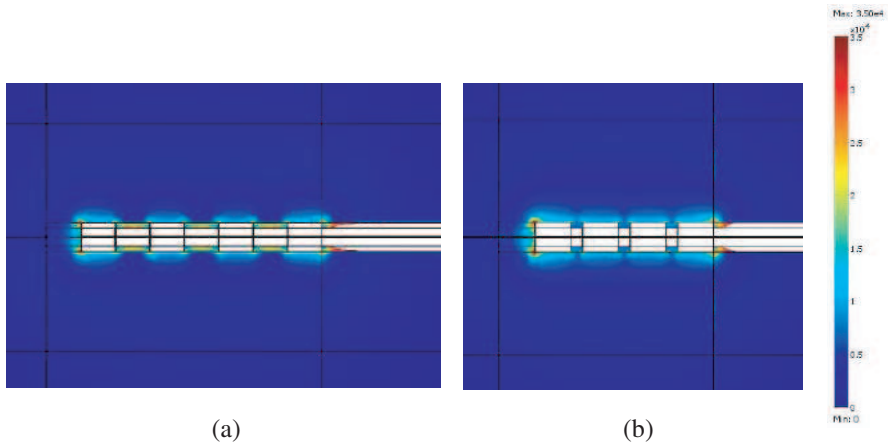
Figure 7. Spatial electric field (V/m) distribution for: (a) L_2. (b) L_4. The color scale on the right is for both colormaps.

total RF field $(\mathbf{E}, \mathbf{H})$ in the presence of an implant satisfies

$$\vec{\nabla} \times \vec{\nabla} \times \mathbf{E} + j\omega\mu_0 \left(\sigma + j\omega\varepsilon\right)\mathbf{E} = -j\omega\mu_0\mathbf{J} \qquad (2)$$

where $\mathbf{J} = \left[(\sigma_i - \sigma) + j\omega(\varepsilon_i - \varepsilon)\right]\mathbf{E}$ in the implant region, where σ_i and ε_i are the conductivity and permittivity respectively of the implant material (these are functions of position over the implant region), and $\mathbf{J} = 0$ in tissue. Since the incident field is available inside body tissue, the MR source need not be included in the computational domain. The air-tissue interface effect is negligible, a fact that is well-known for
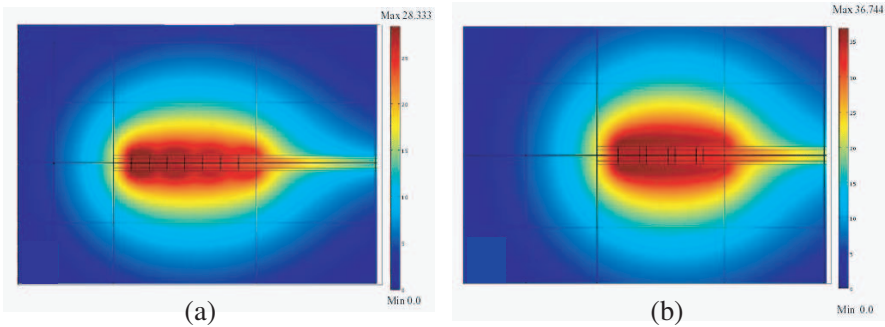
Figure 8. Spatial temperature rise distribution in degrees Celsius after 6 minutes of application of RF input power for: (a) L_2 (b) L_4.
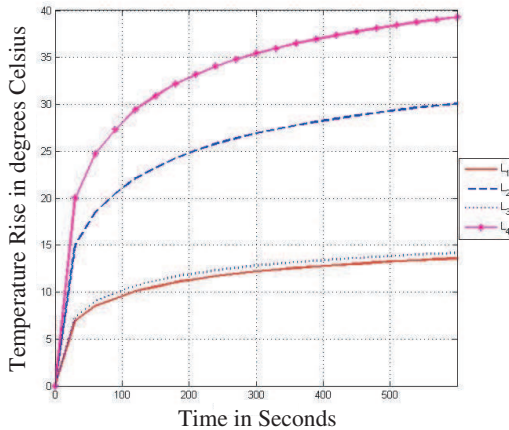
Figure 9. Temperature rise (in degrees Celsius) versus time (in seconds) plots. Plots are at a point ($r = 0.635\,\text{mm} + 0.4\,\text{mm}$, $x = 2.25\,\text{mm}$), that is, $0.4\,\text{mm}$ from surface of the distal metal electrode.

MRI scattering computations [26, 27]. These considerations form part of the second-stage formulation in which FEM has been used for the computation of the resultant RF field as well as for solving the bioheat equation. A computational domain was chosen with its boundaries at least four cm from the implanted lead. Comsol Multiphysics has been used as the FEM based software tool. The results obtained are presented in Fig. 3, and Figs. 5 to 9.

4. RESULTS AND DISCUSSION

The instantaneous power in an elemental tissue volume of length dL and cross-sectional area dS is

$$P_i = (\sigma \mathbf{E} dS) \cdot (\mathbf{E} dL) \qquad \text{(Watts)} \qquad (3)$$

where $\mathbf{E}$ is the instantaneous electric field, and σ is the tissue conductivity at the considered point. Note that $\sigma \mathbf{E}$ is the current density, $\sigma \mathbf{E} dS$ is the instantaneous current flowing through the elemental cross-section dS, and $\mathbf{E} dL$ is the instantaneous voltage drop along the elemental length dL. The real power dissipated as heat is the time-average value of P_i and is

$$P_a = (1/2)\sigma E_m^2 dS dL \qquad \text{(Watts)} \qquad (4)$$

where E_m is the amplitude of the electric field. Clearly P_a is the local heat source in an elemental tissue volume $dV = dS dL$, and can also be expressed as

$$P_a = \rho_m \, (\text{SAR}) \, dV \qquad \text{(Watts)} \qquad (5)$$

where ρ_m is the mass density of tissue and SAR is the specific absorption rate. From (4) and (5) we see that the SAR is given by

$$\text{SAR} = \sigma E_m^2 / (2\rho_m) \qquad \text{(W/kg)} \qquad (6)$$

SAR is a standard measure of the resistive heating that occurs in tissue. Note that (6) gives the local SAR at a point. The local SAR at a point is defined as the power dissipated as heat per unit mass of tissue. This may be integrated over a tissue region having a total mass M (kg) occupying a total volume V (m^3) for obtaining a mass-averaged value of SAR,

$$\text{SAR}_{average} = \frac{1}{V} \int\limits_V \frac{\sigma E_m^2}{2\rho_m} dV \qquad \text{(W/kg)} \qquad (7)$$

Figure 3 shows plots of the local SAR against distance measured along a line that runs in tissue parallel to the central cylindrical axis of a lead. This line, shown in dashed red in an inset at the top of each plot, is chosen so that it runs very close to the electrodes' surface. The

lateral distance of the electrodes' surface from this line is only 0.5 mm. The four peaks in the local SAR values in each plot correspond to those parts of the line where it is parallel to and almost adjacent to the surfaces of the four metal electrodes.

Figure 4 shows various radial lines (in red) intersecting the lead's central cylindrical axis (i.e., the x-axis) at right angles so that $r = 0$ at each point of intersection. We note that the coordinate x has a certain value at this point of intersection and if we change x then the point of intersection also shifts, that is, the position of a radial line also changes. Of course r is the distance measured along a radial line. The value of r increases from zero to more positive values as we move outwards along a radial line on either side of the $r = 0$ point. Fig. 4 shows four different radial lines, ℓ_1, ℓ_2, ℓ_3, and ℓ_4; each radial line is at a constant value of x. The four different radial lines represent the following cases:

- The radial line crosses the proximal metal electrode. ℓ_1 and ℓ_2 are such lines and are shown in Fig. 4. For $\mathbf{L}_1$ and $\mathbf{L}_2$, which are different lengths of the 3387 lead, we have chosen $x = 11.5$ mm and the corresponding radial line is ℓ_1 in Fig. 4(a). For $\mathbf{L}_3$ and $\mathbf{L}_4$, which are different lengths of the 3389 lead, we have chosen $x = 8.5$ mm and the corresponding radial line is ℓ_2 in Fig. 4(b). For the lead $\mathbf{L}_2$, a plot of the local SAR against distance r measured along ℓ_1 is shown in Fig. 5(a). For the lead $\mathbf{L}_4$, a plot of the local SAR against distance r measured along ℓ_2 is shown in Fig. 5(b). For the leads $\mathbf{L}_1$ and $\mathbf{L}_3$, the plots are similar to those for $\mathbf{L}_2$ and $\mathbf{L}_4$ respectively, but the SAR values are lower, the respective peak values being 1.5×10^4 and 1.58×10^4 W/kg. These lower values can be attributed to the smaller lengths of $\mathbf{L}_1$ and $\mathbf{L}_3$, because, based on wavelength considerations, the lengths of $\mathbf{L}_2$ and $\mathbf{L}_4$ are closer to the resonant lengths [13]. In both the plots of Fig. 5, it can be seen that a sharp discontinuity in the SAR value occurs at the metal-tissue interface; the SAR goes from zero inside the metal (because the electric field is zero inside the perfect electric conductor representing metal) to a very high value in the

Table 1. Decay in the SAR values with distance. The values are for $\mathbf{L}_4$.

r (mm)	2.5	3	3.4	4	4.6	5	5.5
Local SAR (W/kg)	1326	750	541	321	228	168	128
r (mm)	6.1	7	8	9	10	12	15
Local SAR (W/kg)	95	61.5	40	26.7	19.2	10.5	5.1

brain tissue adjoining the metal surface. It should be noted that although the total tangential electric field is zero at the metal-tissue interface, the normal electric field there has a very high value. Also the decay in the SAR value as we move in tissue away from the electrode's surface is very rapid. At $r = 0.75$ mm (just 0.1 mm away from the electrode's surface), the rate of change is as high as 8.77×10^4 and 8.94×10^4 W/kg^{-1} mm^{-1} for $\mathbf{L}_2$ and $\mathbf{L}_4$ respectively. Table 1 gives some values for $\mathbf{L}_4$ which cannot be read from the scale for SAR in Fig. 5. These SAR variations agree well with the spatial electric field distributions in Fig. 7. Since SAR $\propto |\mathbf{E}|^2$, a very strong electric field exists at the surface of each metal electrode and the adjacent tissue; the highest values occur at each electrode's tips as can be seen in Fig. 7. The total electric field *inside* the metal electrodes and the metal portion connecting them is zero so the SAR there is also zero. These metal regions appear white in Fig. 7.

- The radial line crosses the insulation tip at the distal end. ℓ_3 and ℓ_4 are such lines and are shown in Fig. 4. We have chosen $x = 0.8$ mm for both ℓ_3, and ℓ_4. Fig. 4(a) shows the position of ℓ_3 and Fig. 4(b) shows ℓ_4. For the lead $\mathbf{L}_2$, a plot of the local SAR against distance r measured along ℓ_3 is shown in Fig. 6(a). For the lead $\mathbf{L}_4$, a plot of the local SAR against distance r measured along ℓ_4 is shown in Fig. 6(b). For $\mathbf{L}_1$ and $\mathbf{L}_3$, the plots are similar to those for $\mathbf{L}_2$ and $\mathbf{L}_4$ respectively, but the SAR values are lower, the respective peak values being 1800 and 2215 W/kg. The local SAR inside the insulation is zero and it jumps to a high value in brain tissue, although *this high value in tissue adjacent to the insulation is much less than that in tissue adjacent to a metal electrode.* This can be seen by comparing Fig 6(a) to Fig 5(a), and Fig. 6(b) to Fig 5(b): $4270 \ll 3.7 \times 10^4$ for $\mathbf{L}_2$ and $5860 \ll 4.45 \times 10^4$ W/kg for $\mathbf{L}_4$. *The reasons for the local SAR being zero in the insulation and being zero inside the metal (PEC) are very different.* The SAR inside the metal (PEC) is zero because the electric field there is zero, but the electric field inside the insulation has very high values – indeed these values are even higher than those in some of the brain tissue adjacent to parts of the metal electrodes (as can be seen in the spatial plot of Fig. 7); however, the conductivity of the insulation is zero and hence the SAR there is zero. In other words, a very high RF electric field can be maintained inside the insulation since it is a lossless dielectric having no conduction losses. The large magnitude of the RF electric field intensity that exists inside the insulation means that the insulation used in the lead should be of a very good quality.

Note that the connecting portion is much longer than the electrodes' portion, by a factor that can be from about 25 to 50. The length of the connecting portion of the lead is very important because the closer it is to the resonant length, the higher will be the strength of the scattered wave propagating inside the long insulating sheath which forms the exterior of the connecting portion of the lead. Thus a very strong RF electric field exists inside this insulation sheath. The lead is like a coaxial transmission line, the lead's metallic wires playing the role of the inner conductor of the coax, the surrounding tissue acting like the outer conductor of the coax, and the lead wires' insulation along with the long outer insulating sheath acting as the dielectric separating the inner and outer conductors of the coax [13]. The power losses along the length of the lead (that is, the connecting portion) are small: these are resistive losses in the tissue surrounding the connecting portion. However most of the wave energy is carried through the insulation to the electrodes' portion at the end where it is dissipated as heat in the tissue surrounding the electrodes. The length at which maximum heating occurs is the resonant length and that is determined from the MR frequency and the nature of the embedding tissue.

The spatial temperature rise distributions (in degrees Celsius) after six minutes of continuous application of RF power are shown in Fig. 8. The temperature rise at the electrode nearer to the distal end is seen to be a few degrees higher than at the proximal electrode. Fig. 9 shows plots of temperature rise, T, against time, t, for the leads $\mathbf{L}_1$ thru $\mathbf{L}_4$ when MRI input power is turned on at the time instant $t = 0$; the temperature rise is measured at a point P ($r = 1.035\,\mathrm{mm}$, $x = 2.25\,\mathrm{mm}$) near the surface of the distal electrode. Let T_0 be the temperature rise after 6 minutes at the point P, where T_0 can be read at the time instant $t = 360$ seconds from the plots in Fig. 9 (for $\mathbf{L}_1$ thru $\mathbf{L}_4$). We now consider cylindrical tissue volumes surrounding the electrodes. The central axis of each cylindrical volume is the x-axis. The power dissipated in each tissue volume is obtained by integrating $\mathrm{Re}(1/2)\sigma\mathbf{E}.\mathbf{E}^*$ over the volume. Table 2 specifies the dissipated powers P_1 and P_2 and the corresponding volumes V_1 and V_2. Table 3 gives the values of P_1 and P_2. The quantity P_1/T_0 depends on the shape of the electrodes and the structure of the lead's electrodes portion. It may be considered as a parameter characterizing the lead's electrodes. P_1/T_0 is almost constant for different values of the MRI input power and for different lengths of a particular type of lead. Thus $\mathbf{L}_1$ and $\mathbf{L}_2$ which are different lengths of the 3387 lead have almost the same value of P_1/T_0; similarly $\mathbf{L}_3$ and $\mathbf{L}_4$ which are different lengths of the 3389 lead have almost the same value of P_1/T_0.

Table 4 gives the $\mathrm{SAR}_{average}$ values over the volumes V_1 and V_2

Table 2. Meanings of the powers P_1 and P_2.

	For $\mathbf{L_1}$ and $\mathbf{L_2}$	For $\mathbf{L_3}$ and $\mathbf{L_4}$
$P_1 = \int_{V_1} \mathrm{Re}\,\frac{1}{2}(\sigma\mathbf{E} \cdot \mathbf{E*})\,dV$ (Watts)	$V_1 : 0 < r < 1\,\mathrm{cm},$ $-1\,\mathrm{cm} < x < 2.2\,\mathrm{cm}$	$V_1 : 0 < r < 1\,\mathrm{cm},$ $-1\,\mathrm{cm} < x < 1.9\,\mathrm{cm}$
$P_2 = \int_{V_2} \mathrm{Re}\,\frac{1}{2}(\sigma\mathbf{E} \cdot \mathbf{E*})\,dV$ (Watts)	$V_2 : 0 < r < 0.5\,\mathrm{cm},$ $-0.5\,\mathrm{cm} < x < 1.2\,\mathrm{cm}$	$V_2 : 0 < r < 0.5\,\mathrm{cm},$ $-0.5\,\mathrm{cm} < x < 0.9\,\mathrm{cm}$

Table 3. Power dissipated as heat around the electrodes (see Table 2 for the meanings of P_1 and P_2).

Lead	P_1 (W)	P_2 (W)	P_2/P_1 (%)	P_1/T_0 (mW/°C)
$\mathbf{L_1}$	0.587897	0.459237	78.1	46.8
$\mathbf{L_2}$	1.319796	1.021157	77.4	47.5
$\mathbf{L_3}$	0.566518	0.436147	77.0	43.0
$\mathbf{L_4}$	1.578328	1.206751	76.5	43.2

Table 4. The mass-averaged SAR. The value in parantheses (in gms) is the mass of brain tissue surrounding the DBS electrodes over which the local SAR is averaged.

Lead	$\mathrm{SAR}_{average}$ (W/kg)	$\mathrm{SAR}_{average}$ (W/kg)
$\mathbf{L_1}$	58.48 (10.1 gms)	344 (1.3 gms)
$\mathbf{L_2}$	131.28 (10.1 gms)	764.8 (1.3 gms)
$\mathbf{L_3}$	62.18 (9.1 gms)	396.6 (1.1 gms)
$\mathbf{L_4}$	173.2 (9.1 gms)	1097.4 (1.1 gms)

for the leads $\mathbf{L_1}$ to $\mathbf{L_4}$, where $\mathrm{SAR}_{average}$ is defined in Eq. (7). We can define a mass-averaged SAR concentration factor, C_a (dimensionless), as the ratio of $\mathrm{SAR}_{average}$ to the background SAR in brain tissue. C_a, being a normalized quantity, can serve as a useful measure for characterizing a lead.

5. CONCLUSIONS

The RF field that exists in body tissue during MRI is very intense in the vicinity of the electrodes of an implanted DBS lead. This results in a concentration of the specific absorption rate around the electrodes. The level of this concentration depends on the overall

length of the lead and the nature of the embedding tissue. The spatial SAR distribution determines the degree of the localized heating that occurs. The mass-averaged value of the SAR determines the average degree of heating. The SAR concentration factor can serve as a useful measure for characterizing the RF induced heating capability of a lead.

REFERENCES

1. Zhang, Y., S. Wang, and L. Wu, "A novel method for magnetic resonance brain image classification based on adaptive chaotic PSO," *Progress In Electromagnetics Research*, Vol. 109, 325–343, 2010.

2. Rezai, A. R., D. Finelli, J. A. Nyenhuis, G. Hrdlicka, J. Tkach, A. Sharan, P. Rugieri, P. H. Stypulkowski, and F. G. Shellock, "Neurostimulation systems for deep brain stimulation: In vitro evaluation of magnetic resonance imaging-related heating at 1.5 T," *J. Magn. Reson. Imaging*, Vol. 15, No. 3, 241–250, Mar. 2002.

3. Dormont, D., P. Cornu, B. Pidoux, et al., "Chronic thalamic stimulation with three-dimensional MR stereotactic guidance," *AJNR Am J. Neuroradiol*, Vol. 18, 1093–1097, 1997.

4. Gemio, J., J. Parron, and J. Soler, "Human body effects on implantable antennas for ism bands applications: Models comparison and propagation losses study," *Progress In Electromagnetics Research*, Vol. 110, 437–452, 2010.

5. Iero, D., T. Isernia, A. F. Morabito, I. Catapano, and L. Crocco, "Optimal constrained field focusing for hyperthermia cancer therapy: A feasibility assessment on realistic phantoms," *Progress In Electromagnetics Research*, Vol. 102, 125–141, 2010.

6. Christopoulou, M., S. Koulouridis, and K. S. Nikita, "Parametric study of power absorption patterns induced in adult and child head models by small helical antennas," *Progress In Electromagnetics Research*, Vol. 94, 49–67, 2009.

7. Biagi, P. F., L. Castellana, T. Maggipinto, G. Maggipinto, T. Ligonzo, L. Schiavulli, D. Loiacono, A. Ermini, M. Lasalvia, G. Perna, and V. Capozzi, "A reverberation chamber to investigate the possible effects of 'in vivo' exposure of rats to 1.8 GHz electromagnetic fields: A preliminary study," *Progress In Electromagnetics Research*, Vol. 94, 133–152, 2009.

8. Nyenhuis, J. A., S. M. Park, R. Kamondetdacha, A. Amjad, F. G. Shellock, and A. Rezai, "MRI and implanted medical

devices: Basic interactions with an emphasis on heating," *IEEE Trans. Device and Materials Reliability*, Vol. 5, No. 3, Sep. 2005.

9. Islam, M. T., M. R. I. Faruque, and N. Misran, "Design analysis of ferrite sheet attachment for SAR reduction in human head," *Progress In Electromagnetics Research*, Vol. 98, 191–205, 2009.

10. Chou, H.-H., H.-T. Hsu, H.-T. Chou, K.-H. Liu, and F.-Y. Kuo, "Reduction of peak SAR in human head for handset applications with resistive sheets (R-cards)," *Progress In Electromagnetics Research*, Vol. 94, 281–296, 2009.

11. Manapati, M. B. and R. S. Kshetrimayum, "SAR reduction in human head from mobile phone radiation using single negative metamaterials," *Journal of Electromagnetic Waves and Applications*, Vol. 23, No. 10, 1385–1395, 2009.

12. Hirata, A., H. Sugiyama, and O. Fujiwara, "Estimation of core temperature elevation in humans and animals for whole-body averaged SAR," *Progress In Electromagnetics Research*, Vol. 99, 53–70, 2009.

13. Mohsin, S. A., N. M. Sheikh, and U. Saeed, "MRI induced heating of deep brain stimulation leads," *Physics in Medicine & Biology*, Vol. 53, 5745–5756, 2008.

14. Park, S. M., R. Kamondetdacha, A. Amjad, and J. A. Nyenhuis, "MRI safety: RF induced heating on straight wires," *IEEE Trans. Magn.*, Vol. 41, No. 10, 4197–4199, Oct. 2005.

15. Park, S. M., "MRI safety: Radiofrequency field induced heating of implanted medical devices," Ph.D. Thesis, Purdue University, 2006.

16. Harrington, R. F., *Field Computation by Moment Methods*, Wiley-Interscience and IEEE Press Series on Electromagnetic Wave Theory, 1993.

17. Taflove, A. and S. C. Hagness, *Computational Electrodynamics: The Finite-Difference Time-Domain Method*, 3rd edition, Artech House, Norwood, MA, 2005.

18. Sullivan, D. M., *Electromagnetic Simulation Using the FDTD Method*, IEEE Press Series on RF and Microwave Technology, 2000.

19. Volakis, J. L., A. Chatterjee, and L. C. Kempel, *Finite Element Method for Electromagnetics*, The IEEE/OUP Series on Electromagnetic Wave Theory, 2002.

20. Jin, J. M., *The Finite Element Method in Electromagnetics*, 2nd edition, John Wiley and Sons, 2002.

21. Lancellotti, V., B. P. de Hon, and A. G. Tijhuis, "Scattering from

large 3-d piecewise homogeneous bodies through linear embedding via green's operators and arnoldi basis functions," *Progress In Electromagnetics Research*, Vol. 103, 305–322, 2010.

22. Mohsin, S. A., "A simple EM model for determining the scattered magnetic resonance radiofrequency field of an implanted medical device," *Progress In Electromagnetics Research M*, Vol. 14, 1–14, 2010.

23. Amjad, A., "Specific absorption rate during magnetic resonance imaging," Ph.D. Thesis, Purdue University, 2007.

24. Amjad, A., R. Kamondetdacha, A. V. Kildishev, S. M. Park, and J. A. Nyenhuis, "Power deposition inside a phantom for testing of MRI heating," *IEEE Trans. Magn.*, Vol. 41, 4185–4187, 2005.

25. Mohsin, S. A., N. M. Sheikh, F. Mahmood, and W. Abbas, "General considerations regarding scattering of the MRI RF field by implanted medical devices," *Pakistan Journal of Engineering and Applied Sciences*, Vol. 6, 17–25, Jan. 2010.

26. Mohsin, S. A., N. M. Sheikh, and U. Saeed, "MRI induced heating of deep brain stimulation leads: Effect of the air-tissue interface," *Progress In Electromagnetics Research*, Vol. 83, 81–91, 2008.

27. Mohsin, S. A., J. Nyenhuis, and R. Masood, "Interaction of medical implants with the MRI electromagnetic fields," *Progress In Electromagnetics Research C*, Vol. 13, 195–202, 2010.